

Fast control of the transverse structure of a light beam using acousto-optic modulators

MAHDIEH CHARTAB JABBARI^{1,*}, CHENG LI¹, XIALIN LIU¹, R. MARGOTH CÓRDOVA-CASTRO¹, BORIS BRAVERMAN^{1,3}, JEREMY UPHAM^{1,2}, AND ROBERT W. BOYD^{1,2}

¹Department of Physics, University of Ottawa, Ottawa, ON, K1N6N5, Canada

²Institute of Optics, University of Rochester, Rochester, New York 14620, United States

³Department of Physics, University of Toronto, Toronto, ON, M5S1A7, Canada

*mchar380@uottawa.ca

Compiled July 16, 2024

Fast, reprogrammable control over the transverse structure of light beams plays an essential role in applications such as structured illumination microscopy, optical trapping, and quantum information processing. Existing technologies, such as liquid crystal on silicon spatial light modulators (LCoS-SLMs) and digital micromirror devices (DMDs), suffer from limited refresh rates, low damage thresholds, and high insertion loss. Acousto-optic modulators (AOMs) can resolve the above issues, as they typically handle higher laser power and offer lower insertion loss. By effectively mapping the temporal radio-frequency (RF) waveforms onto the spatial diffraction patterns of the optical field, individual AOMs have been shown to generate one-dimensional (1D) spatial modes at a pixel refresh rate of nearly 20 MHz [1]. We extend this concept to enable fast modulation in a two-dimensional (2D) space using a double-AOM scheme. We demonstrate the generation of 2D Hermite-Gaussian (HG_{nm}) modes with an average fidelity of 81%, while the highest-order mode generated, HG_{53} , retains a fidelity of 56%.

<http://dx.doi.org/10.1364/ao.XX.XXXXXX>

1. INTRODUCTION

Generation and manipulation of spatial light modes enables a wide range of applications. Accessing multiple spatial modes allows information encoding in a higher dimension, thereby boosting the capacity of quantum information processing [2–4]. The ability to shape optical wavefronts helps create complex optical traps, enabling novel optical tweezers and laser material processing technologies [5, 6].

Diffraction optical elements such as LCoS-SLMs and mechanical optical components such as DMDs are typically used to generate and manipulate the spatial structure of light. LCoS-SLMs offer high resolution and programmable modulation, but they are typically limited to a refresh rate of around 120 Hz due to the long response time of liquid crystal molecules. The use

of liquid crystals also results in low damage thresholds of the orders of microjoules per square centimeter [7–9]. In contrast, DMDs, composed of an array of microelectromechanical mirrors, can achieve refresh rates of up to 22 kHz [1, 10], but they exhibit higher insertion loss than LCoS-SLMs.

Acousto-optic modulators (AOMs), consisting of crystals driven by piezoelectric transducers, offer remarkable benefits in modulating spatial modes of light and can potentially overcome the limitations mentioned above [11]. LCoS-SLMs update the generated spatial mode in a time interval on the order of several ms [8, 9, 12], while AOMs can modulate at frequencies up to tens of MHz, constrained only by the sound waves' transit time across the beam waist. This fast refresh rate makes AOMs suitable for applications that require high-speed modulation, such as laser-scanning microscopy and optical communications [13, 14]. Furthermore, typical materials comprising AOMs, such as fused silica (SiO_2) and tellurium dioxide (TeO_2), offer significantly higher optical damage thresholds of the order of joules per square centimeter, which make AOMs capable of handling high-power laser beams. The diffraction efficiency of AOMs typically ranges from 50% to 90% or higher, exceeding that of DMDs [15, 16]. Unlike LCoS-SLMs, which are sensitive to the polarization of incident laser beams, the AOMs' diffraction efficiency is unaffected by the polarization [17, 18].

Spatial light modulation using AOMs has found applications in various fields. Treptow et al. eliminate common coherent artifacts in holography by harnessing the intrinsic motion of acousto-optic holograms [19]. A double-pass AOM, functioning as a fast steerable mirror with a high switching rate, facilitates rapid state tomography of spatial modes within a 2-dimensional Hilbert space [9]. Recent developments in acousto-optic systems have also shown potential in random-access scanning, ultrafast confocal and multiphoton imaging, as well as fast inertia-free light-sheet microscopy [13, 20, 21].

So far, AOMs have been used mainly to modulate light in a one-dimensional (1D) space. To access the full potential of AOM-based spatial light modulation, a scheme for independent control over orthogonal components of the optical field in a two-dimensional (2D) space is needed. This paper proposes and demonstrates a double AOM scheme that modulates an optical beam in both orthogonal transverse directions. We demon-

strate 2D spatial light modulation by generating and detecting Hermite Gaussian (HG_{nm}) modes up to a total mode order of $n+m = 8$. By optimizing the input RF waveform, the fidelity of the generated modes to the target modes reaches an average of 81%. Although the fidelity decreases with increasing mode order, the highest order mode, HG_{53} , poses a fidelity of 56%. The limit to the mode order we were able to generate, and the corresponding drop-off in mode fidelity is due to technical limitations of this experimental setup (principally AOM aperture) rather than any fundamental limitation of this approach.

2. PRINCIPLES OF OPERATION

Fig. 1(a) is a schematic of an AOM in which a piezoelectric transducer propagates a known RF waveform as a sound wave through a quartz crystal. The compression pattern induced by the sound wave creates a spatially varying refractive index, illustrated by a false color pattern. This refractive index pattern acts as a diffraction grating that imprints a spatial structure onto the diffracted beam. Adjusting the amplitude and frequency of the RF waveform manipulates the amplitude and phase of this beam. AOMs typically accommodate RF drive frequencies between 50 to 200 MHz range [1].

Light diffraction by an AOM obeys Bragg's Law. The first-order diffraction, which exhibits the highest efficiency, is generated at an angle θ given by

$$\sin \theta = \frac{\lambda_0}{n\lambda_s} = \frac{\lambda_0 f}{nv_s}, \quad (1)$$

where λ_0 and λ_s represent the wavelengths of the light in vacuum and sound, respectively, n stands for the refractive index of the crystal, v_s is the propagation velocity of sound, and f is the carrier frequency of the RF waveform. To achieve the highest diffraction efficiency, the input beam should enter the AOM at the Bragg angle, $\theta_B = \theta/2$ [22].

The time-dependent amplitude of the RF waveform is mapped directly onto the intensity profile of the optical beam, while the variation of RF frequency modulates the phase pattern. Since beam components diffracted into different angles accumulate phase differences as they propagate along different paths inside the AOM, we can obtain the desired 1D modulation of the complex field amplitude at the output plane by controlling the temporal variation of RF frequency driving the AOM.

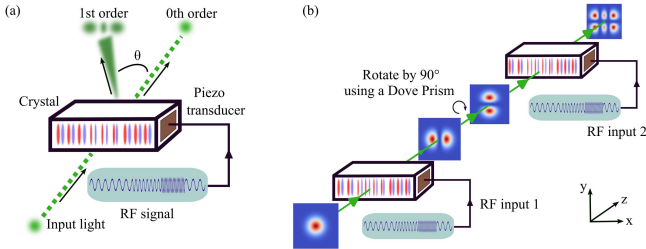


Fig. 1. (a) A schematic diagram of AOM-based spatial light modulation. Blue and red false-color blobs show the crystal being compressed or stretched by the acoustic wave. (b) Principle of generating 2D structured patterns from two 1D modulations.

To enable light modulation in the 2D space, one can use two AOMs that independently modulate the beams in perpendicular directions. However, arranging two AOMs perpendicular

to one another over-complicates the experimental setup and degrades its stability. Instead, we rotate the beam diffracted by the first AOM by 90 degrees using a Dove prism (DP) before sending it to the second AOM, as illustrated in Fig. 1(b). We denote the transfer matrices of the first and second AOMs as \hat{U}_{x1} and \hat{U}_{x2} , and that of DP as a rotation operator \hat{R} . The output field can then be expressed as

$$E_o = \hat{U}_{x2} \hat{R} \hat{U}_{x1} E_i, \quad (2)$$

where E_i represents the input optical field; notice that the y-direction modulation is realized by a rotated x-direction modulation, namely, $\hat{U}_y = \hat{R} \hat{U}_x$. This approach essentially enables light modulation in both the x- and y-directions, $E_o = \hat{U}_x \hat{U}_y E_i$, while keeping the two AOMs aligned in parallel.

It is important to note that spatial light modulation using an AOM is only functional if the laser pulse duration is significantly shorter than the shortest period of the acoustic waves inside the crystal. The spatial mode would be distorted and blurred by the movement of the acoustic pattern inside the crystal [1].

3. EXPERIMENTAL RESULTS

Fig. 2 shows the schematic of our experimental setup. A laser (Thorlabs NPL52B) emits light pulses with a duration of 10 ns at a wavelength of 520 nm and a repetition rate determined by external triggering up to 10 MHz. Light pulses are first coupled into a single-mode fiber to ensure a Gaussian-shape spatial profile. Subsequently, the light is coupled out into free space and split into two paths, denoted signal and reference.

Since both AOMs have rectangular apertures of 7 mm by 2 mm, the signal beam is expanded into an elliptical shape using an anamorphic prism pair (APP₁) to fit into AOM₁. The elliptical beam, diffracted and modulated by AOM₁, is first restored to a circular shape by APP₂ and then rotated by 90 degrees using a Dove prism shaped again into elliptical and sent into AOM₂. The modulated beam is then restored to a circular shape by APP₄. A 4-f imaging system, comprised of lenses L₁ and L₂ with a focal length of 100 mm, positions AOM₂ in the near-field of AOM₁. The AOMs are driven independently by RF signals sent from different output ports of an arbitrary waveform generator (AWG, Keysight M8195A). An opaque beam block (BB) blocks the zeroth-order diffraction from each AOM. The first-order diffracted light is collimated using lenses L₃ and L₄, with focal lengths of 50 mm and 75 mm, respectively, and then directed to the rest of the setup. Lenses L₅ and L₆, with focal lengths of 15 mm and 125 mm, respectively, expand the reference beam in a Galilean telescope configuration, which a beam splitter then recombines with the structured signal beam. A CCD camera positioned in the near field of the second AOM captures the interference pattern. The complex field distribution of the signal field is then retrieved using digital off-axis holography [23].

Fig. 3(a) shows the generated 2D HG_{nm} modes for $n = 0$ to 5 and $m = 0$ to 3, up to the highest total mode order of $N = n + m = 8$. The refractive index patterns within the AOM may not replicate the RF waveform for very large modulation frequencies, causing phase distortions in the diffracted beam. The distortions can be avoided using RF waveforms with slowly varying amplitude and phase. However, modulating arbitrary transverse patterns requires dealing with abrupt phase changes, such as the π -phase shifts in HG modes, that could induce sig-

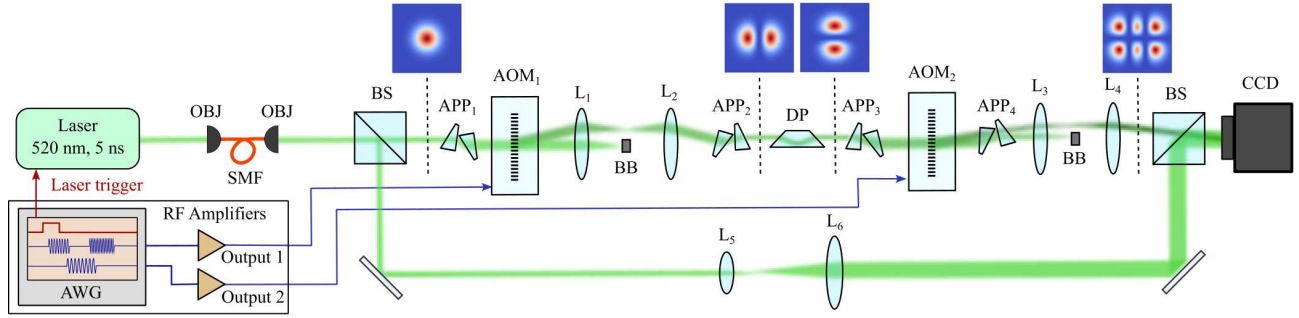


Fig. 2. Schematic of the experimental setup. SMF: single-mode fiber, BS: beam splitter, APP: anamorphic prism pair, BB: beam block, DP: Dove prism. The insets show the mode profiles being modified towards the target mode, HG₂₁.

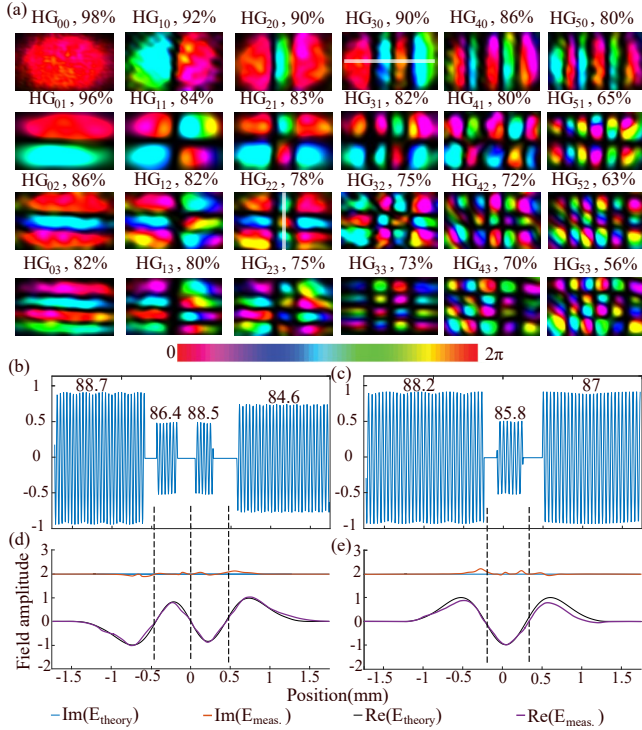


Fig. 3. (a) Experimentally generated HG modes. Saturation and hue represent the intensity and phase of the field, respectively. (b) RF waveform $f(x_2)$ loaded onto AOM₂ to modulate the x-component of HG₃₀ and (c) $f(x_1)$ loaded on AOM₁ to modulate the y-component of HG₂₂. Numbers indicate the corresponding RF frequency (MHz) in each waveform segment. Cross-sections of the measured and theoretical profiles of the field amplitude at the output of the AOM (d) for HG₃₀ and (e) for HG₂₂, with the positions of the cuts in the experimental data shown by white lines in (a). The imaginary components are vertically offset by two units for enhanced visualization.

nificant deviations between the output field (E_o) and the target field (E_t).

We implement the following optimization scheme to maximize mode fidelity. Recall that $E_o = \hat{U}_{x_2} \hat{R} \hat{U}_{x_1} E_i$. The transfer matrix \hat{U} is a function of the position-dependent amplitude $A(d)$ and phase $\phi(d)$ of the light field. Since $A(d)$ approximately replicates the amplitude of the RF waveform, the majority of the optimization is performed on $\phi(d)$, which relates to the position-dependent detuning from the Bragg frequency

$\Delta f(d)$ through

$$\phi(d) \sim \frac{d}{v_s} \Delta f(d), \quad (3)$$

where d indicates the position in the AOM along the propagation direction of the sound wave. The output field is then written as $E_o[f(x_1), f(x_2)] = \hat{U}_{x_2}[f(x_2)]\hat{U}_{x_1}[f(x_1)]E_i$. The optimization procedure is now formulated as jointly iterating $f(x_1)$ and $f(x_2)$, the RF frequency components in two AOMs, for a maximum mode overlap given by $|E_t E_o|^2 / (|E_t|^2 |E_o|^2)$ namely,

$$f(x_1), f(x_2) = \operatorname{argmax}_{f(x_1), f(x_2)} \frac{|E_t \cdot E_o[f(x_1), f(x_2)]|^2}{|E_t|^2 \cdot |E_o[f(x_1), f(x_2)]|^2}. \quad (4)$$

These norms are computed through integration over space, ensuring an accurate representation of the field distributions. Experimentally, the RF waveform is optimized as follows. We first divide the RF signal into segments whose relative amplitudes and regions replicate that of the target HG mode's 0- and π -phase sections. To keep the amplitude of each segment constant, we independently tune the RF frequency across a 30 MHz range centered on the Bragg frequency of 86 MHz for our AOMs, using 0.1 MHz steps. Fig. 3(b) shows the optimized RF waveform $f(x_2)$ loaded on AOM₂ to modulate the input beam in the x-direction and generate the HG₃₀ mode. Each of the four distinct sections of an HG₃₀ mode corresponds to a segment of the RF waveform with a different frequency. Each segment is sequentially optimized individually. We scale the RF amplitude in different segments to compensate for the uneven amplitude of the beam caused by its Gaussian profile. To account for the varying diffraction efficiencies between lobes, we adjust each segment's width without optimization to achieve the desired amplitude modulation in the output. Fig. 3(d) illustrates the real and imaginary parts of the optimized mode and a comparison with the theoretical mode profiles, yielding a mode fidelity of 90%. The white lines in Fig. 3(a) indicate the cross-section where the mode profiles are plotted. For 2D HG modes, we conduct the same procedure for y-direction modulation after optimizing for the x-direction. Figure 3(c) shows the optimized RF waveform $f(x_1)$ loaded onto AOM₁ that carries out the y-direction modulation for generating HG₂₂. The overall 2D mode fidelity is 78%.

Fig. 4 illustrates the fidelity in creating the desired mode for total mode order $n + m$. While increasing mode order is associated with lower fidelities, the highest order mode we studied, HG₅₃, possesses a fidelity of 56%. We attribute the decrease in fidelity to two major factors. First, the diffraction efficiency could saturate and distort the intensity profile in the modulated

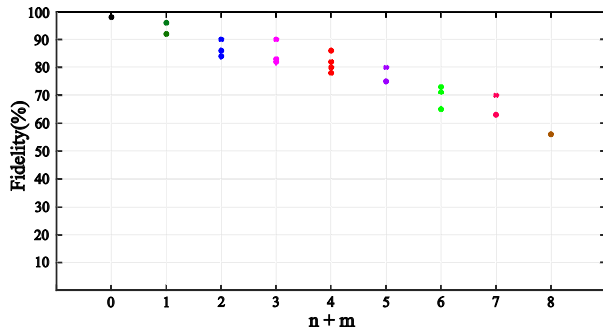


Fig. 4. Dependence of the fidelity of the generated mode on the sum $n + m$ of the mode indices.

beam, or it could drop when the RF frequencies deviate from the Bragg frequency. These effects are more significant in modulating higher-order modes, where RF waveforms must contain multiple frequency components. We measure the diffraction efficiencies of AOM₁ and AOM₂ to be 90% and 82%, respectively, at the Bragg RF frequency. As a result, the diffraction efficiency of HG₀₀ is 73%; whereas at the highest order mode generated, HG₅₃, the total diffraction efficiency drops to 13%. The second factor is the limited spatial resolution, which is determined by the total number of acoustic wavelengths that fit within the AOM aperture. This quantity is given by a product of δt , the time duration for an acoustic wave to traverse the AOM's aperture, and δf , the RF modulation bandwidth of the AOM [24]. If we denote the aperture size as l , then the unit effective pixel size of our AOM is given as

$$\frac{l}{\delta t \delta f} = \frac{l}{(l/v_s)\delta f} = \frac{v_s}{\delta f}. \quad (5)$$

With an RF bandwidth of 30 MHz and an acoustic velocity of 3.63 mm/ μ s, we estimate an effective unit pixel size of 120 μ m, equivalent to 57 pixels across the 7 mm aperture. As the mode order increases, HG modes display finer spatial features whose sizes approach that of the AOM pixels. However, we argue that the limitation of 120 μ m pixel size is not fundamental to AOM-based spatial modulation systems and a higher fidelity and maximal mode order is achievable using AOMs with larger clear apertures and RF bandwidths.

Although our system is designed to work with spatial modes that are separable in the x - and y -components, the setup can access a much larger Hilbert space beyond the 24 modes shown in Fig. 3(a). For instance, Laguerre-Gaussian (LG) modes can be generated by adding an HG to LG mode converter [25].

4. CONCLUSION

In conclusion, we demonstrate 2D spatial light modulation using a double AOM system. Specifically, we successfully demonstrate the generation of any of the 24 distinct spatial modes at high speeds, all sharing a common structural characteristic in two spatial dimensions. The modulation rate with suitable electronics would be approximately 500 kHz, considering that the transit time of sound across the 7 mm aperture is about 2 microseconds. It is important to note that while we focus on these 24 modes, the total Hilbert space accessible by our system is significantly larger. The AOM-based spatial light modulation systems of a similar kind can potentially offer pixel refresh rates of

nearly 20 MHz, as reported in earlier work [1]. By optimizing the RF waveform, we achieve an 81% average mode fidelity. Using AOMs with optimized RF bandwidth and larger apertures can improve the resolution of the AOM-based spatial light modulation system and further boost the mode fidelity.

Our approach offers a promising alternative to traditional DMDs and LCoS-SLMs, which are prone to damage when modulating intense, short optical pulses. Notably, rapid data acquisition is critical in achieving high time resolution in dynamic imaging. Our system can thus potentially facilitate various dynamic imaging techniques, including in-vivo speckle imaging and random illumination microscopy.

Funding. Natural Sciences and Engineering Research Council of Canada; Canada Research Chairs; Canada First Research Excellence Fund award on Transformative Quantum Technologies.

Acknowledgement. R.W.B. thanks the US Office of Naval Research, the US National Science Foundation under Award 2138174, the National Research Council Canada New Beginning Initiative Ideation Fund, and the US Department of Energy under award FWP 76295. B.B. acknowledges the support of the Banting postdoctoral fellowship of NSERC.

Disclosures. The authors declare no conflicts of interest.

Data availability. The data are available from the corresponding authors upon reasonable request.

REFERENCES

- X. Liu, B. Braverman, and R. W. Boyd, *Opt. Express* **31**, 1501 (2023).
- K. H. Kagalwala, G. Di Giuseppe, A. F. Abouraddy, and B. E. Saleh, *Nat. communications* **8**, 739 (2017).
- F. Brandt, M. Hiekkamäki, F. Bouchard, M. Huber, and R. Fickler, *Optica* **7**, 98 (2020).
- G. B. Xavier and G. Lima, *Commun. Phys.* **3**, 9 (2020).
- Y. Yang, Y.-X. Ren, M. Chen, Y. Arita, and C. Rosales-Guzmán, *Adv. Photonics* **3**, 034001 (2021).
- A. Möhl, S. Kaldun, C. Kunz, F. A. Müller, U. Fuchs, and S. Gräf, *J. Laser Appl.* **31**, 042019 (2019).
- Z. Xing, W. Fan, D. Huang, H. Cheng, and G. Xia, *Opt. Lett.* **45**, 3537 (2020).
- S. Turtaev, I. T. Leite, K. J. Mitchell, M. J. Padgett, D. B. Phillips, and T. Čižmár, *Opt. Express* **25**, 29874 (2017).
- B. Braverman, A. Skerjanc, N. Sullivan, and R. W. Boyd, *Opt. Express* **28**, 29112 (2020).
- K. J. Mitchell, S. Turtaev, M. J. Padgett, T. Čižmár, and D. B. Phillips, *Opt. Express* **24**, 29269 (2016).
- A. I. Chizhikov, V. Y. Molchanov, N. F. Naumenko, and K. B. Yushkov, "Acousto-optic spatial light modulator (slm) based on KYW crystal," in *Laser Beam Shaping XX*, vol. 11486 (SPIE, 2020), pp. 50–55.
- C. Zhou, C. He, S.-T. Yan, Y.-H. Ji, L. Zhou, J. Wang, and M.-S. Zhan, *Rev. Sci. Instruments* **91** (2020).
- M. Duocastella, S. Surdo, A. Zunino, A. Diaspro, and P. Saggau, *J. Physics: Photonics* **3**, 012004 (2020).
- A. A. Pohl, R. A. Oliveira, R. E. Da Silva, C. A. Marques, P. d. T. Neves, K. Cook, J. Canning, and R. N. Nogueira, *Photonic Sensors* **3**, 1 (2013).
- X. Zhang, Y. Chen, J. Fang, T. Wang, J. Li, and L. Luo, *Opt. Express* **27**, 11503 (2019).
- P. A. Nikitin, V. V. Gerasimov, and I. S. Khasanov, *Materials* **15**, 8836 (2022).
- G. Lazarev, A. Hermerschmidt, S. Krüger, and S. Osten, *Opt. Imaging Metrol. Adv. Technol.* pp. 1–29 (2012).
- Y. Igasaki, F. Li, N. Yoshida, H. Toyoda, T. Inoue, N. Mukohzaka, Y. Kobayashi, and T. Hara, *Opt. Rev.* **6**, 339 (1999).
- D. Treptow, R. Bola, E. Martín-Badosa, and M. Montes-USategui, *Sci. Reports* **11**, 21261 (2021).

20. R. Salomé, Y. Kremer, S. Dieudonné, J.-F. Léger, O. Krichevsky, C. Wyart, D. Chatenay, and L. Bourdieu, *J. neuroscience methods* **154**, 161 (2006).
21. M. Duocastella, G. Sancataldo, P. Saggau, P. Ramoino, P. Bianchini, and A. Diaspro, *ACS Photonics* **4**, 1797 (2017).
22. B. E. Saleh and M. C. Teich, *Fundamentals of photonics* (John Wiley & Sons, 2019).
23. J. H. Massig, *Opt. letters* **27**, 2179 (2002).
24. M. Dugan, J. Tull, and W. Warren, *JOSA B* **14**, 2348 (1997).
25. D. Shen, T. He, X. Yu, and D. Zhao, *IEEE Photonics J.* **14**, 1 (2022).

FULL REFERENCES

1. X. Liu, B. Braverman, and R. W. Boyd, "Using an acousto-optic modulator as a fast spatial light modulator," *Opt. Express* **31**, 1501–1515 (2023).
2. K. H. Kagalwala, G. Di Giuseppe, A. F. Abouraddy, and B. E. Saleh, "Single-photon three-qubit quantum logic using spatial light modulators," *Nat. communications* **8**, 739 (2017).
3. F. Brandt, M. Hiekkamäki, F. Bouchard, M. Huber, and R. Fickler, "High-dimensional quantum gates using full-field spatial modes of photons," *Optica* **7**, 98–107 (2020).
4. G. B. Xavier and G. Lima, "Quantum information processing with space-division multiplexing optical fibres," *Commun. Phys.* **3**, 9 (2020).
5. Y. Yang, Y.-X. Ren, M. Chen, Y. Arita, and C. Rosales-Guzmán, "Optical trapping with structured light: a review," *Adv. Photonics* **3**, 034001–034001 (2021).
6. A. Möhl, S. Kaldun, C. Kunz, F. A. Müller, U. Fuchs, and S. Gräf, "Tailored focal beam shaping and its application in laser material processing," *J. Laser Appl.* **31**, 042019 (2019).
7. Z. Xing, W. Fan, D. Huang, H. Cheng, and G. Xia, "High laser damage threshold liquid crystal optical switch based on a gallium nitride transparent electrode," *Opt. Lett.* **45**, 3537–3540 (2020).
8. S. Turtaev, I. T. Leite, K. J. Mitchell, M. J. Padgett, D. B. Phillips, and T. Čížmár, "Comparison of nematic liquid-crystal and dmd based spatial light modulation in complex photonics," *Opt. Express* **25**, 29874–29884 (2017).
9. B. Braverman, A. Skerjanc, N. Sullivan, and R. W. Boyd, "Fast generation and detection of spatial modes of light using an acousto-optic modulator," *Opt. Express* **28**, 29112–29121 (2020).
10. K. J. Mitchell, S. Turtaev, M. J. Padgett, T. Čížmár, and D. B. Phillips, "High-speed spatial control of the intensity, phase and polarisation of vector beams using a digital micro-mirror device," *Opt. Express* **24**, 29269–29282 (2016).
11. A. I. Chizhikov, V. Y. Molchanov, N. F. Naumenko, and K. B. Yushkov, "Acousto-optic spatial light modulator (slm) based on KYW crystal," in *Laser Beam Shaping XX*, vol. 11486 (SPIE, 2020), pp. 50–55.
12. C. Zhou, C. He, S.-T. Yan, Y.-H. Ji, L. Zhou, J. Wang, and M.-S. Zhan, "Laser frequency shift up to 5 ghz with a high-efficiency 12-pass 350-mhz acousto-optic modulator," *Rev. Sci. Instruments* **91** (2020).
13. M. Duocastella, S. Surdo, A. Zunino, A. Diaspro, and P. Saggau, "Acousto-optic systems for advanced microscopy," *J. Physics: Photonics* **3**, 012004 (2020).
14. A. A. Pohl, R. A. Oliveira, R. E. Da Silva, C. A. Marques, P. d. T. Neves, K. Cook, J. Canning, and R. N. Nogueira, "Advances and new applications using the acousto-optic effect in optical fibers," *Photonic Sensors* **3**, 1–25 (2013).
15. X. Zhang, Y. Chen, J. Fang, T. Wang, J. Li, and L. Luo, "Beam pointing stabilization of an acousto-optic modulator with thermal control," *Opt. Express* **27**, 11503–11509 (2019).
16. P. A. Nikitin, V. V. Gerasimov, and I. S. Khasanov, "Acousto-optic modulation and deflection of terahertz radiation," *Materials* **15**, 8836 (2022).
17. G. Lazarev, A. Hermerschmidt, S. Krüger, and S. Osten, "Lcos spatial light modulators: trends and applications," *Opt. Imaging Metrol. Adv. Technol.* pp. 1–29 (2012).
18. Y. Igasaki, F. Li, N. Yoshida, H. Toyoda, T. Inoue, N. Mukohzaka, Y. Kobayashi, and T. Hara, "High efficiency electrically-addressable phase-only spatial light modulator," *Opt. Rev.* **6**, 339–344 (1999).
19. D. Treptow, R. Bola, E. Martín-Badosa, and M. Montes-Usategui, "Artifact-free holographic light shaping through moving acousto-optic holograms," *Sci. Reports* **11**, 21261 (2021).
20. R. Salomé, Y. Kremer, S. Dieudonné, J.-F. Léger, O. Krichevsky, C. Wyart, D. Chatenay, and L. Bourdieu, "Ultrafast random-access scanning in two-photon microscopy using acousto-optic deflectors," *J. neuroscience methods* **154**, 161–174 (2006).
21. M. Duocastella, G. Sancataldo, P. Saggau, P. Ramoino, P. Bianchini, and A. Diaspro, "Fast inertia-free volumetric light-sheet microscope," *ACS Photonics* **4**, 1797–1804 (2017).
22. B. E. Saleh and M. C. Teich, *Fundamentals of photonics* (John Wiley & sons, 2019).
23. J. H. Massig, "Digital off-axis holography with a synthetic aperture," *Opt. letters* **27**, 2179–2181 (2002).
24. M. Dugan, J. Tull, and W. Warren, "High-resolution acousto-optic shaping of unamplified and amplified femtosecond laser pulses," *JOSA B* **14**, 2348–2358 (1997).
25. D. Shen, T. He, X. Yu, and D. Zhao, "Mode conversion and transfer of orbital angular momentum between hermite-gaussian and laguerre-gaussian beams," *IEEE Photonics J.* **14**, 1–6 (2022).